Crystal and magnetic structure of the complex oxides Sr_2MnMoO_6, Sr_2MnWO_6 and Ca_2MnWO_6: a neutron diffraction study

2002 J. Phys.: Condens. Matter 14 8817

(http://iopscience.iop.org/0953-8984/14/38/306)

INSTITUTE OF PHYSICS PUBLISHING JOURNAL OF PHYSICS: CONDENSED MATTER

J. Phys.: Condens. Matter **14** (2002) 8817–8830 PII: S0953-8984(02)34402-3

Crystal and magnetic structure of the complex oxides Sr_2MnMoO_6, Sr_2MnWO_6 and Ca_2MnWO_6: a neutron diffraction study

A Muñoz[1,4], J A Alonso[2], M T Casais[2], M J Martínez-Lope[2] and M T Fernández-Díaz[3]

[1] Dpto Física Aplicada, EPS, Universidad Carlos III, Avda Universidad, 30, Leganés-Madrid E-28911, Spain
[2] Instituto de Ciencia de Materiales de Madrid, CSIC, Cantoblanco, E-28049 Madrid, Spain
[3] Institut Laue-Langevin, BP 156X, Grenoble, F-38042, France

E-mail: amunoz@fis.uc3m.es

Received 28 February 2002
Published 12 September 2002
Online at stacks.iop.org/JPhysCM/14/8817

Abstract

A study of the crystallographic and magnetic structure of the double perovskites Sr_2MnMoO_6, Sr_2MnWO_6 and Ca_2MnWO_6 has been carried out on polycrystalline samples using neutron powder diffraction (NPD) data. A room temperature analysis of high-resolution NPD patterns has shown that these compounds crystallize, at room temperature, in the monoclinic space group $P2_1/n$. The three perovskites contain divalent Mn cations. Ca_2MnWO_6 presents the strongest distortion with respect to the ideal cubic perovskite structure. The low-temperature antiferromagnetic ordering has been followed from sequential NPD data. The magnetic structures are defined by the propagation vectors $\boldsymbol{k} = (1/2, 0, 1/2)$ for Sr_2MnMoO_6 and Sr_2MnWO_6, and $\boldsymbol{k} = (0, 1/2, 1/2)$ for Ca_2MnWO_6. The possible arrangements for the Mn^{2+} magnetic moments have been derived from a group theory analysis.

1. Introduction

In the last few years a great effort has been devoted to the study of the hole-doped rare-earth manganites $R_{1-x}A_xMnO_3$ (A = alkaline earth) [1, 2], with the aim of achieving a better understanding of the mechanisms involved in the colossal-magnetoresistance (CMR) effect observed in these perovskite oxides. This intensive work has also been driven by the possible technological applications of these materials in magnetoelectronic devices, stimulating the search for new CMR compounds. Recently, it has been reported that Sr_2FeMoO_6 double perovskite presents CMR properties, at temperatures significantly above room temperature [3].

[4] Author to whom any correspondence should be addressed.

Soon, similar CMR properties were described for other complex perovskites, such as Sr_2FeReO_6 and Ba_2FeMoO_6 [4–8], triggering research on other complex oxides. In these double perovskites, the CMR effect is only observed in polycrystalline specimens, and it seems to be due to an extrinsic effect originating at the grain boundaries, so-called tunnelling magnetoresistance [9]. The motion of the carriers across the grain boundaries is controlled by the external magnetic field by its aligning the magnetic moments of the grain surface.

The ideal structure of the compounds belonging to the $A_2BB'O_6$ family, where A stands for an alkaline-earth ion and B and B′ are transition metal ions, can be viewed as a regular arrangement of corner-sharing BO_6 and $B'O_6$ octahedra, alternating along the three directions of the crystal, with the large A cations occupying the voids in between the octahedra. A rock-salt-like structure is thus observed in the B-cation sublattice. Depending on the relative size of the B and B′ cations with respect to the A atoms, the crystal structure has been defined either as cubic ($Fm\bar{3}m$), tetragonal ($I4/m$) or monoclinic ($P2_1/n$). For instance, Sr_2FeMoO_6 is cubic above the ferrimagnetic Curie temperature, and it undergoes a structural phase transition and becomes tetragonal ($I4/m$) below this temperature [11–13]. Ca_2FeMoO_6 is monoclinic [14], showing a significant tilt of the FeO_6 and MoO_6 octahedra, given the small size of the Ca cations placed at A positions.

The Mn analogues of Sr_2FeMoO_6 have attracted our attention. The double perovskites Sr_2MnMoO_6 and Sr_2MnWO_6 were first studied in the 1960s. Sr_2MnMoO_6 was described as cubic with $a = 7.98$ Å [15]; an antiferromagnetic behaviour was observed below $T_N = 12$ K [16]. Sr_2MnWO_6 was originally reported as cubic with $a = 8.01$ Å [17]; more recently the structure has been refined in the tetragonal $P42/n$ space group, describing an antiferromagnetic ordering below $T_N = 10$ K [18]. A recent neutron diffraction study [19] has shown that Ca_2MnWO_6 is monoclinic ($P2_1/n$), undergoing a transition to an antiferromagnetic structure below $T_N = 16$ K.

In the present work we describe the synthesis of these materials, prepared by 'chimie douce' procedures, and the results of high-resolution neutron powder diffraction (NPD) studies on well crystallized samples. The crystal structures of Sr_2MnMoO_6 and Sr_2MnWO_6 have been revisited: we report complete structural data for these monoclinically distorted perovskites. The possible magnetic structures compatible with the symmetry of the compounds have been obtained by following the group theory analysis.

2. Experimental details

The Sr_2MnMoO_6, Sr_2MnWO_6 and Ca_2MnWO_6 perovskites were prepared as brown polycrystalline powders from citrate precursors obtained by soft-chemistry procedures. Stoichiometric amounts of analytical grade $Sr(NO_3)_2$ or $CaCO_3$; $MnCO_3$; and $(NH_4)_6Mo_7O_{24}{\cdot}4H_2O$ or $H_{26}N_6O_{41}W_{12}{\cdot}18H_2O$ were dissolved in citric acid. The citrate + nitrate solutions were slowly evaporated, leading to organic resins containing a random distribution of the cations involved at an atomic level. These resins were first dried at 120 °C and then slowly decomposed at temperatures up to 600 °C. All the organic materials and nitrates were eliminated in a subsequent treatment at 800 °C in air, for 2 h. They were then treated at 1000 °C for 12 h in air. Finally, the oxides were reduced under an H_2/N_2 flow (15%/85%) at 1050 °C for 8 h (W perovskites) or 1000 °C for 8 h (Mo perovskite).

For each compound, a high-resolution NPD pattern was collected at room temperature at the D2B diffractometer of the Institut Laue-Langevin in Grenoble (France), with a wavelength of 1.594 Å. The 2Θ angular range covered by the diffractometer was 5°–162° with a step size of 0.05°. For the study of the magnetic structure and its thermal evolution a set of NPD patterns were acquired at the D20 multidetector (1600 counters) diffractometer, with a wavelength

Table 1. Lattice parameters at room temperature.

	Sr_2MnMoO_6	Sr_2MnWO_6	Ca_2MnWO_6
a (Å)	5.6671(1)	5.6803(2)	5.4694(2)
b (Å)	5.6537(1)	5.6723(2)	5.6504(2)
c (Å)	7.9969(2)	8.0199(2)	7.8122(3)
β (deg)	89.927(2)	89.936(3)	90.179(3)
Volume (Å^3)	256.22(1)	258.41(1)	241.43(2)

$\lambda = 2.40$ Å. The useful 2Θ angular range covered was 1.0°–154.5° with a step size of 0.10°. The sequential diagrams were collected every 2 K from 2 to 40 K and then every 10 K from 40 to 70 K. The refinements of the crystallographic and the magnetic structures were performed by using the Rietveld method with the FULLPROF program [20]. In the profile refinements, the peak shape was simulated by a pseudo-Voigt function and the background was fitted with a fifth-degree polynomial function.

3. Results and discussion

3.1. Crystallographic structure

The crystal structure refinement was performed on the D2B high-resolution data collected at room temperature and with a wavelength $\lambda = 1.594$ Å. In the three compounds the Bragg reflections were indexed with a monoclinic unit cell and the structures were refined in the monoclinic space group $P2_1/n$. Since $SrWO_4$ and $CaWO_4$ were detected as minor impurities in Sr_2MnWO_6 and Ca_2MnWO_6, respectively, they were included as secondary phases in the final refinement. The compounds AWO_4 (A = Sr, Ca) are tetragonal (space group $I4_1/a$). From the scale factors of the main and secondary phases, we estimated 3% of $SrWO_4$ in Sr_2MnWO_6 and 6% of $CaWO_4$ in Ca_2MnWO_6. The good agreement between the observed and calculated patterns after the refinement is shown in figure 1. The lattice parameters and the final atomic coordinates of the different compounds are reported in tables 1 and 2, respectively. The mean interatomic distances and some selected bond angles are listed in table 3.

In a recent study of the crystallographic structure of Sr_2MnWO_6 [19], the tetragonal space group $P4_2/n$ has been proposed. In this description, it is necessary to consider three different positions for the Sr atoms and the volume of the tetragonal cell is nearly twice the monoclinic volume. With our experimental data we have carried out a fitting of the crystallographic structure of the three compounds with the $P4_2/n$ space group. The fitting is only possible for Sr_2MnMoO_6 and Sr_2MnWO_6. The R-factors obtained in the fitting are $R_{Bragg} = 5.5$ and $\chi^2 = 2.6$ for Sr_2MnMoO_6 and $R_{Bragg} = 7.4$ and $\chi^2 = 2.1$ for Sr_2MnWO_6. These discrepancy factors are slightly worse than those obtained for $P2_1/n$, given in table 2. The unit-cell volumes are 512.17(2) and 516.67(2) Å^3 for Sr_2MnMoO_6 and Sr_2MnWO_6, respectively. As the structure can be described in $P2_1/n$ with a smaller unit cell, with considerably fewer atoms per unit cell and variable parameters, we preferred the monoclinic description for these compounds.

The monoclinic space group $P2_1/n$ allows for two different octahedral sites, which can be occupied by the B and B′ atoms (B = Mn and B′ = Mo or W). In this case, the Mn and Mo or W atoms are fully ordered in each site, in such a way that each MnO_6 octahedron is linked to six $B'O_6$ octahedra, as can be seen in figure 2. The B and B′ ions are arranged alternately forming a rock-salt sublattice.

In both Sr_2MnMoO_6 and Sr_2MnWO_6 unit cells the monoclinic distortion is very small, with β-angles very close to 90°; this effect has been widely observed in many 1:1 ordered

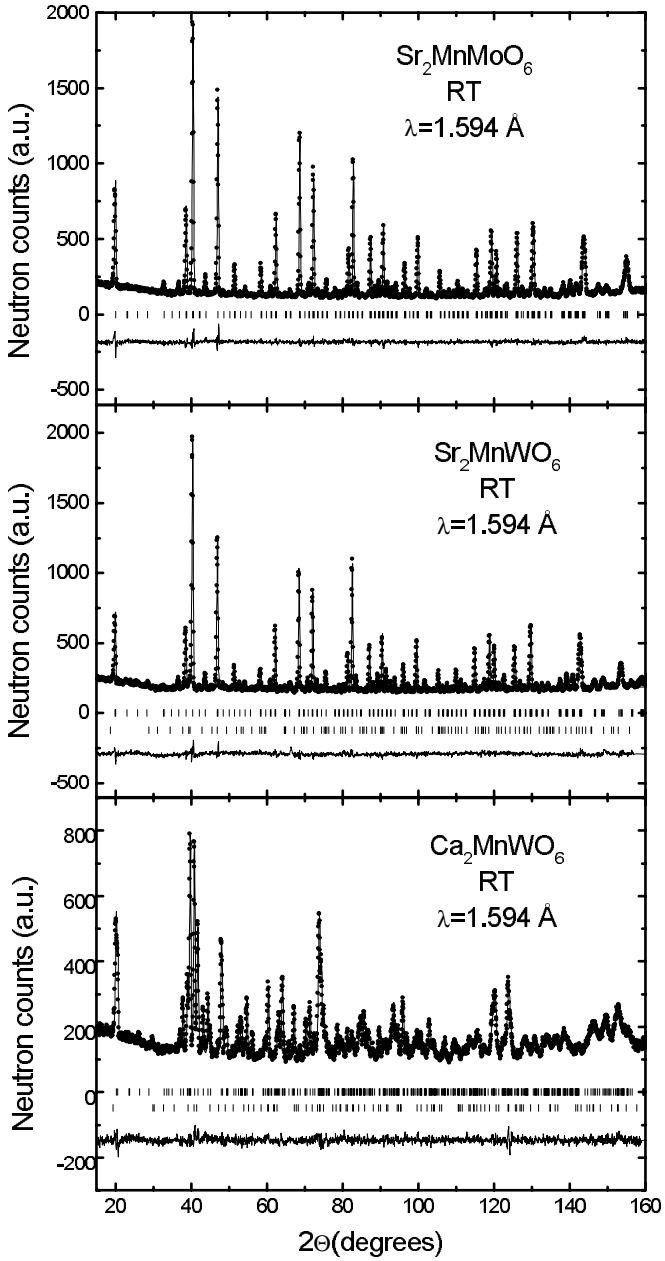

Figure 1. Observed (solid circles), calculated (solid curve) and difference (bottom curve) high-resolution NPD patterns. The first row of tick marks correspond to the Bragg reflections of the monoclinic space group $P2_1/n$ of the $A_2MnB'O_6$ (B′ = Mo or W) phase and the second to the AWO_4 impurities (A = Sr, Ca).

perovskites with a strong pseudo-orthorhombic character. The size of the unit cell is slightly larger for Sr_2MnWO_6, as expected for the larger W^{6+} ionic radius (0.60 Å) versus Mo^{6+} (0.59 Å) in octahedral coordination. For Ca_2MnWO_6 the monoclinic distortion is more important

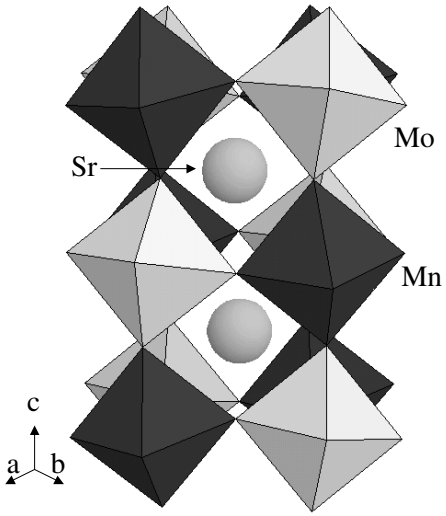

Figure 2. A view of the monoclinic structure of the Sr_2MnMoO_6 double perovskite, highlighting the tilting of the MnO_6 and MoO_6 octahedra.

Table 2. Structural parameters obtained from the Rietveld refinement of the NPD pattern at room temperature with $\lambda = 1.594$ Å. Space group $P2_1/n$. A = Sr, Ca and B′ = Mo, W.

Atoms		Sr_2MnMoO_6	Sr_2MnWO_6	Ca_2MnWO_6
A	x	0.9962(6)	0.9984(9)	0.9877(7)
	y	0.0176(5)	0.0185(6)	0.0535(6)
	z	0.2498(8)	0.2456(12)	0.2542(5)
	B (Å^2)	0.94(4)	0.76(5)	0.77(5)
Mn			(1/2, 0, 0)	
	B (Å^2)	1.16(14)	0.35(15)	0.29(8)
B′			(1/2, 0, 1/2)	
	B (Å^2)	0.51(5)	0.20(11)	0.08(6)
O1	x	0.0546(6)	0.0555(12)	0.0969(5)
	y	0.4937(6)	0.4918(9)	0.4651(5)
	z	0.2363(5)	0.2359(8)	0.2354(4)
	B (Å^2)	0.43(7)	0.85(14)	0.67(5)
O2	x	0.7364(7)	0.7367(10)	0.7141(5)
	y	0.2891(9)	0.2908(12)	0.3136(5)
	z	0.0281(8)	0.0293(12)	0.0453(4)
	B (Å^2)	0.97(8)	0.96(12)	0.62(5)
O3	x	0.2068(7)	0.2030(10)	0.1820(5)
	y	0.2328(8)	0.2302(13)	0.2185(5)
	z	0.9729(7)	0.9717(10)	0.9445(4)
	B (Å^2)	1.03(8)	0.92(11)	0.43(5)
χ^2		1.4	1.7	1.3
R_p		4.1	4.0	4.0
R_{wp}		5.2	5.1	5.1
R_{Bragg}		4.6	7.2	3.6

($\beta = 90.17°$), given the smaller radius for the Ca^{2+} ion with respect to Sr^{2+}; the unit cell is accordingly smaller. Also, in Ca_2MnWO_6 the differences between the lattice parameters a

Table 3. Selected interatomic distances (Å) and selected bond angles (deg).

	Sr_2MnMoO_6	Sr_2MnWO_6	Ca_2MnWO_6
Mn–O1 ($x2$)	2.131(4)	2.142(6)	2.145(3)
Mn–O2 ($x2$)	2.125(4)	2.141(6)	2.153(3)
Mn–O3 ($x2$)	2.131(4)	2.146(6)	2.175(3)
⟨Mn–O⟩	2.129(4)	2.143(6)	2.158(3)
B′–O1 ($x2$)	1.916(4)	1.919(6)	1.922(3)
B′–O2 ($x2$)	1.924(4)	1.923(6)	1.919(3)
B′–O3 ($x2$)	1.924(4)	1.929(7)	1.926(3)
⟨B′–O⟩	1.921(4)	1.924(6)	1.922(3)
A–O1	2.982(4)	3.007(6)	2.406(4)
A–O1	2.714(4)	2.705(6)	3.238(5)
A–O1	2.551(5)	2.543(8)	2.327(5)
A–O2	2.770(7)	2.759(10)	2.654(5)
A–O2	2.560(7)	2.590(11)	2.349(5)
A–O2	2.829(8)	2.860(11)	2.693(5)
A–O3	2.793(8)	2.760(11)	2.804(5)
A–O3	2.803(7)	2.851(9)	2.585(5)
A–O3	2.551(7)	2.520(10)	2.371(5)
⟨A–O⟩	2.728(6)	2.733(9)	2.603(5)
Mn–O1–B′	162.2(2)	161.9(2)	147.60(14)
Mn–O2–B′	162.5(2)	161.9(3)	149.82(14)
Mn–O3–B′	161.5(2)	160.1(3)	146.83(10)

and b are greater, and unlike the case for the Sr compounds, it is verified that $b > a$. This last point, as will be shown later, will play an important role in determining the propagation vector that characterizes its magnetic structure.

It is interesting to note the evolution of the Mn–O interatomic distances (table 3). They are larger in the Ca compound, in spite of the reduction in unit-cell dimensions due to the small Ca^{2+} size. This expansion of Mn–O bond lengths is a result of the competing interactions of Mn–O and Ca–O bonds through common oxygens; the higher electronegativity of Ca^{2+} versus Sr^{2+} accounts for a more covalent (or less ionic) Ca–O bond and a weakening of the Mn–O chemical bonding. For the Sr-containing compounds, the same argument accounts for the slightly larger Mn–O distances in the W versus Mo perovskite: the higher electronegativity of W explains the weakening (lengthening) of the Mn–O bonds through Mn–O–W chemical paths. The tilting angles φ of the MnO_6 and (Mo, W)O_6 octahedra can be simply evaluated as $\varphi = (180 - \phi)/2$, where ϕ is the angle Mn–$\hat{O}$–W. φ noticeably increases from 9.0° and 9.4° for Sr_2MnMoO_6 and Sr_2MnWO_6, respectively, to $\varphi = 16°$ for the much more distorted Ca compound.

3.1.1. Determination of the magnetic structure. The magnetic structure and its thermal evolution were analysed using a set of NPD patterns collected for each compound in the temperature range $2 < T < 40$ K, with $\lambda = 2.40$ Å. As can be observed in figure 3 for the three compounds, new peaks of magnetic origin appear on cooling, which cannot be indexed within the crystallographic $P2_1/n$ space group. They correspond to the onset of a low-temperature magnetic ordering. In Sr_2MnMoO_6 the new peaks appear below $T_N = 15$ K and they can be indexed with the propagation vector $\boldsymbol{k} = (1/2, 0, 1/2)$; in Sr_2MnWO_6 the magnetic reflections appear below $T_N = 13.7$ K and are also indexed with $\boldsymbol{k} = (1/2, 0, 1/2)$; in Ca_2MnWO_6 the new peaks are detected below $T_N = 17$ K, but in this case the propagation

Table 4. Results from the magnetic structure determination for Sr_2MnMoO_6 at $T = 1.8$ K. Magnetic moments are given in μ_B.

Mn(1)	Mn(2)	m_x	m_y	m_z	$\|m\|$	R_{Bragg}	R_{magn}	χ^2
[111]	$[1\bar{1}1]$	2.1(3)	3.0(4)	−2.0(5)	4.17(6)	3.6	7.7	2.1
[111]	$[\bar{1}1\bar{1}]$	1.7(3)	3.5(3)	1.5(5)	4.17(6)	3.7	8.0	2.1
[111]	[111]	1.8(3)	3.3(3)	−1.7(5)	4.17(6)	3.7	7.8	2.1
[111]	$[\bar{1}\bar{1}\bar{1}]$	1.9(3)	3.3(4)	1.7(5)	4.17(6)	3.7	8.0	2.2

Table 5. Results from the magnetic structure determination for Sr_2MnWO_6 at $T = 2.4$ K. Magnetic moments are given in μ_B.

Mn(1)	Mn(2)	m_x	m_y	m_z	$\|m\|$	R_{Bragg}	R_{magn}	χ^2
[111]	$[1\bar{1}1]$	2.5(2)	3.3(2)	−1.7(3)	4.54(6)	5.4	6.3	2.1
[111]	$[\bar{1}1\bar{1}]$	2.3(2)	3.7(2)	1.3(3)	4.54(5)	5.5	6.6	2.1
[111]	[111]	2.3(2)	3.6(2)	−1.4(3)	4.54(5)	5.5	6.2	2.1
[111]	$[\bar{1}\bar{1}\bar{1}]$	2.4(2)	3.5(3)	1.5(3)	4.54(6)	5.4	6.9	2.2

Table 6. Results from the magnetic structure determination for Ca_2MnWO_6 at $T = 1.9$ K. Magnetic moments are given in μ_B.

Mn(1)	Mn(2)	m_x	m_y	m_z	$\|m\|$	R_{Bragg}	R_{magn}	χ^2
[111]	$[1\bar{1}1]$	3.00(11)	1.9(2)	3.4(2)	4.91(5)	4.4	6.0	2.2
[111]	$[\bar{1}1\bar{1}]$	3.00(11)	1.9(2)	3.4(2)	4.91(5)	4.4	6.0	2.2
[111]	[111]	1.9(2)	0.47(9)	4.45(10)	4.86(5)	4.6	7.0	2.3
[111]	$[\bar{1}\bar{1}\bar{1}]$	1.9(2)	−0.46(8)	4.45(10)	4.86(5)	4.6	6.9	2.3

vector is $\boldsymbol{k} = (0, 1/2, 1/2)$. The thermal evolution of the integrated intensity is shown for some magnetic peaks in figure 4.

The possible magnetic structures compatible with the space group symmetry were determined by group theory, as indicated in the appendix. Four models were considered; two of them are those calculated from the representation analysis described in the appendix; the two other models (describing collinear magnetic structures) are obtained by considering a possible mixture of the basis vectors of two irreducible representations. Collinear structures have been considered in preceding papers [18, 19]. These last two solutions must correspond to basis vectors belonging to the same multiplet of the isotropic exchange Hamiltonian and they lead either to a ferromagnetic coupling of the two Mn moments of the unit cell, $\boldsymbol{m}_1 = \boldsymbol{m}_2$, or to an antiferromagnetic coupling, $\boldsymbol{m}_1 = -\boldsymbol{m}_2$. In all cases, we considered that only the Mn^{2+} moments participate in the magnetic ordering, i.e. the oxidation states of Mo and W are 6+, $S = 0$. The results of the fitting are presented in tables 4–6. For the Sr samples, the agreement factors for the experimental data obtained for the four different models are very similar; therefore it is not possible to choose a unique solution. Only for Ca_2MnWO_6 does the model defined by just one irreducible representation seem to present a significantly better agreement with the experimental data.

The best solution for Ca_2MnWO_6 corresponds to the coupling $m_{1x} = -m_{2x}$, $m_{1y} = m_{2y}$ and $m_{1z} = -m_{2z}$ (1 denotes the Mn atom at $(1/2, 0, 0)$ and 2 the Mn atom at $(0, 1/2, 1/2)$). By analogy, this solution has also been adopted for the Sr compounds. The good agreement between the calculated and observed NPD patterns at the lowest temperature is presented in figure 5. The study of the thermal evolution of the NPD diagrams shows that the magnetic

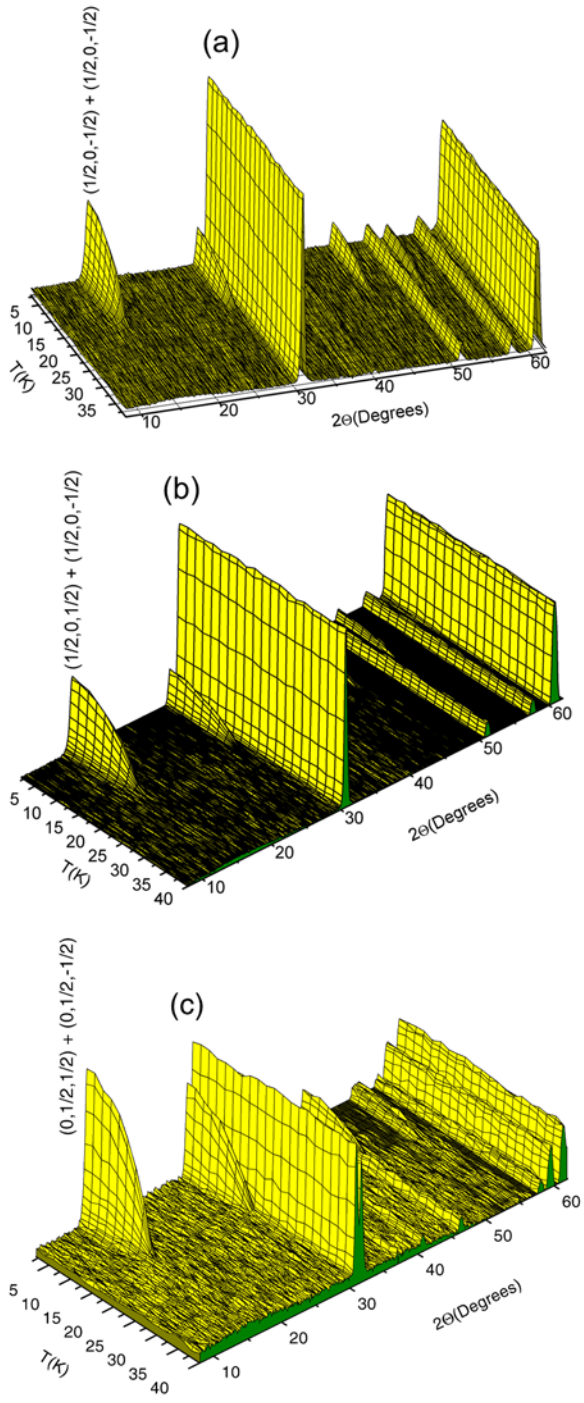

Figure 3. Thermal variation of the NPD patterns acquired with $\lambda = 2.40$ Å in the temperature range $2 < T < 40$ K (a) for Sr_2MnMoO_6, (b) for Sr_2MnWO_6, (c) for Ca_2MnWO_6.

(This figure is in colour only in the electronic version)

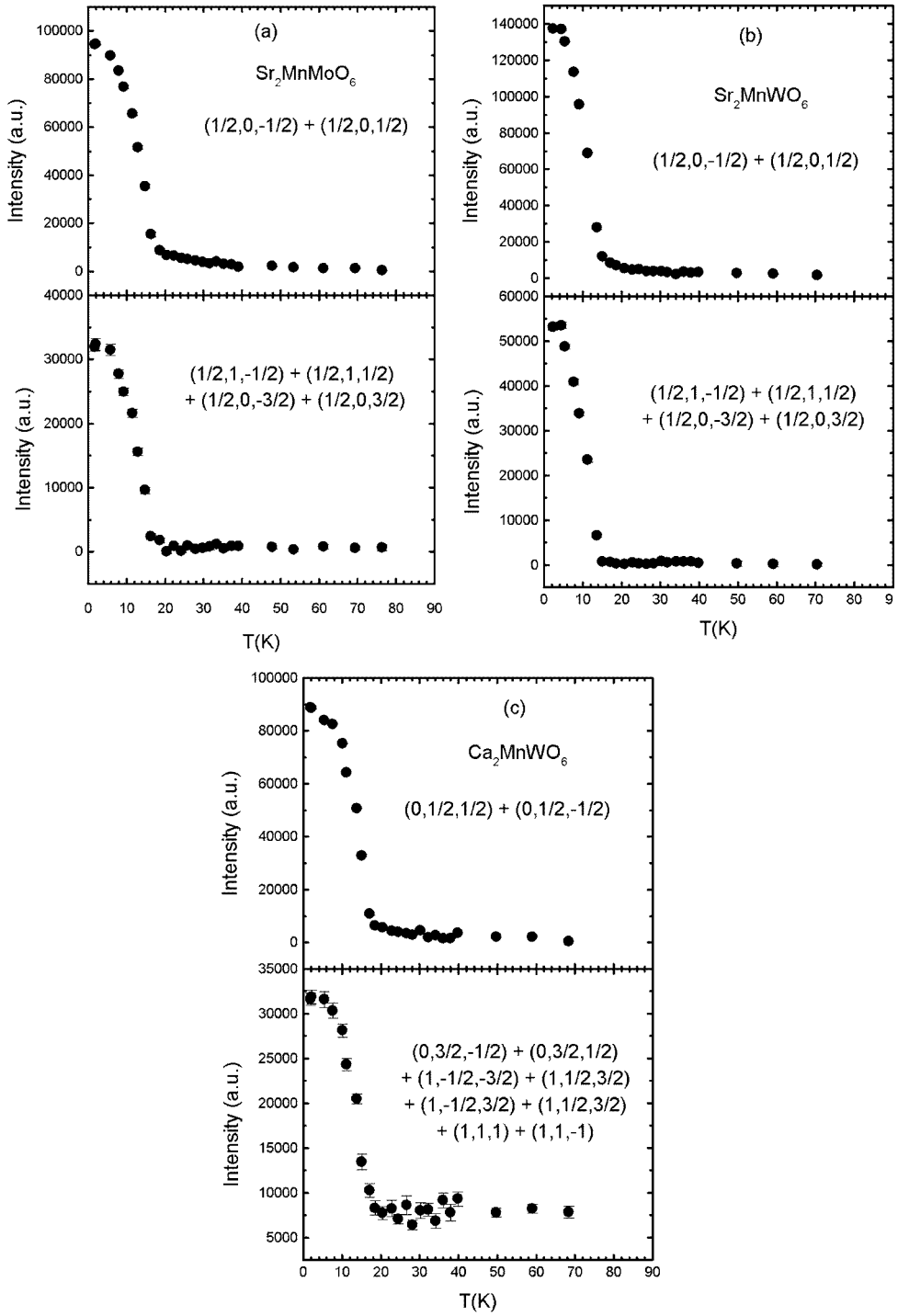

Figure 4. Thermal evolution of the integrated intensities for some magnetic reflections; (a) for Sr_2MnMoO_6, (b) for Sr_2MnWO_6, (c) for Ca_2MnWO_6.

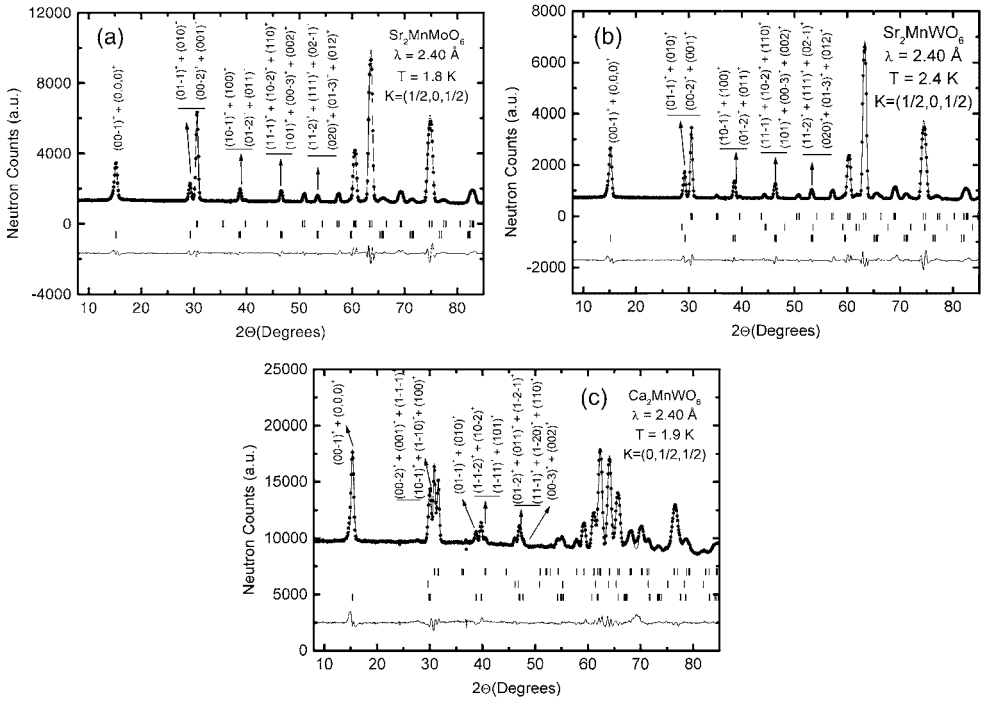

Figure 5. Observed (solid circles), calculated (solid curve) and difference (bottom curve) NPD patterns corresponding to the solution $m_{1x} = -m_{2x}$, $m_{1y} = m_{2y}$ and $m_{1z} = -m_{2z}$. The two series of tick marks correspond to the crystallographic and magnetic Bragg reflections (a) for Sr_2MnMoO_6, (b) for Sr_2MnWO_6, (c) for Ca_2MnWO_6.

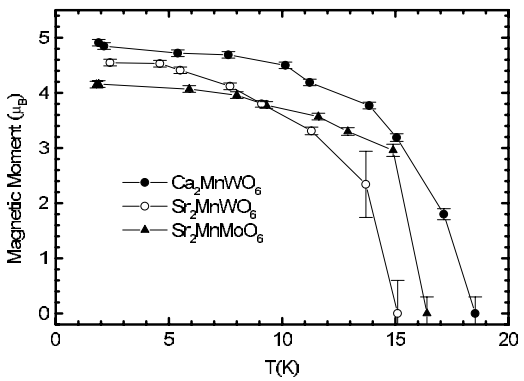

Figure 6. Thermal variation of the magnetic moment for the model $m_{1x} = -m_{2x}, m_{1y} = m_{2y}$ and $m_{1z} = -m_{2z}$.

structure remains stable throughout the temperature range below the ordering temperature. The thermal variations of the magnetic moments are presented in figure 6. A diagram of the magnetic structure for the model considered is presented in figure 7.

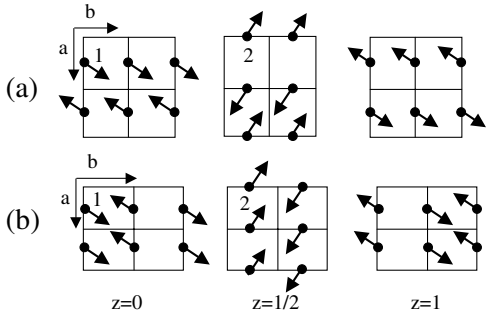

Figure 7. A sketch of the magnetic structure for the model $m_{1x} = -m_{2x}$, $m_{1y} = m_{2y}$ and $m_{1z} = -m_{2z}$ (a) for Sr_2MnMoO_6 and Sr_2MnWO_6 and (b) for Ca_2MnWO_6. The figure shows the projection of the magnetic moments on the $\boldsymbol{a}$–$\boldsymbol{b}$ plane.

3.2. Magnetic structure discussion

The magnetic peaks, and in particular the first magnetic satellite $(000)^+$, disappear at a temperature slightly higher than the reported T_N-values. The ordering temperatures described for Sr_2MnMoO_6, Sr_2MnWO_6 and Ca_2MnWO_6 are, respectively, $T_N = 12$ K [15], 13 K [19] and 16 K [17]; whereas the first magnetic peaks disappear (in the heating runs) at around 15, 13.7 and 17 K, respectively. This slight difference suggests a hysteretic behaviour, or simply the existence of an axial temperature gradient as the cylindrical sample is heated during the dynamic data collection.

In all the cases, the magnetic moment of the Mn ions seems to saturate to a value above 4 μ_B, consistent with a divalent oxidation state of Mn cations ($3d^5$). This implies an oxidation state for the Mo and W ions of Mo^{6+} ($4d^0$) and W^{6+} ($5d^0$), respectively. Therefore, it is consistent with the fact that only the Mn^{2+} moments are ordered and there is no magnetic contribution at the Mo(W) sites. On the order hand, the stronger the structural distortion from the ideal cubic perovskite, the closer the magnetic moment value to 5 μ_B; this is related to the increase in Mn–O atomic distances (as commented on above) and a decrease of the orbital overlap and covalence effects.

The possible magnetic structures obtained in the appendix for each irreducible representation correspond to non-collinear magnetic structures; however, if a mixture of the solutions belonging to different irreducible representations is considered, the magnetic models obtained in this way are collinear. For the Sr samples, the collinear magnetic structures correctly fit the experimental data, leading to discrepancy factors similar to those for the non-collinear structures (tables 4 and 5). The collinear structure implies that the anisotropic terms of the Hamiltonian are much less important than the isotropic ones, which is reasonable as the crystallographic structure is obtained from a subtle distortion of the ideal cubic perovskite to a pseudo-tetragonal one. In the case of the most distorted Ca_2FeMoO_6 perovskite, the collinear magnetic structures lead to slightly worse discrepancy factors (table 6); thus the non-collinear structure is selected and represented in figure 7.

The different propagation vector of the magnetic structures of Sr_2MnMoO_6 and Sr_2MnWO_6 compared to Ca_2MnWO_6 is probably related to the relative lengths in the $\boldsymbol{a}$- and $\boldsymbol{b}$-directions, the $\boldsymbol{a}$-dimension being much shorter for the Ca compound. In the first two materials $\boldsymbol{k} = (1/2, 0, 1/2)$, which implies an antiferromagnetic coupling between the closest Mn^{2+} ions along the $\boldsymbol{a}$- and $\boldsymbol{c}$-directions (see figure 7). In Ca_2MnWO_6 $\boldsymbol{k} = (0, 1/2, 1/2)$ and antiferromagnetic coupling is present along the $\boldsymbol{b}$- and $\boldsymbol{c}$-directions, while the coupling is ferromagnetic along the $\boldsymbol{a}$-axis.

Table A.1. Irreducible representations of the space group $P2_1/n$ for $\boldsymbol{k} = (1/2, 0, 1/2)$. The symmetry elements are written according to Kovalev's notation $\boldsymbol{\tau} = (1/2, 1/2, 1/2)$.

					Basis vectors	
	h_1	$h_{23}/(\tau)$	h_{25}	$h_{27}/(\tau)$	Mn1	Mn2
Γ^1	1	−1	1	−1	—	—
Γ^2	1	−1	−1	1	[1, 1, 1]	[1, $\bar{1}$, 1]
Γ^3	1	1	1	1	—	—
Γ^4	1	1	−1	−1	[1, 1, 1]	[$\bar{1}$, 1, $\bar{1}$]

4. Conclusions

The study of the crystallographic structure of the double perovskites Sr_2MnMoO_6, Sr_2MnWO_6 and Ca_2MnWO_6 using NPD data allowed us to establish that these double perovskites have monoclinic structure, space group $P2_1/n$. The strongest distortion from the ideal cubic perovskite is observed in Ca_2MnWO_6. These compounds experience a low-temperature antiferromagnetic ordering. For Sr_2MnMoO_6 and Sr_2MnWO_6 the magnetic structure is defined by the propagation vector $\boldsymbol{k} = (1/2, 0, 1/2)$ and for Ca_2MnWO_6 the magnetic structure is defined by $\boldsymbol{k} = (0, 1/2, 1/2)$. Neutron data did not allow us to unambiguously establish the magnetic structures at low temperature. It seems clear, however, that only Mn ions are concerned in the magnetic ordering, adopting a divalent oxidation state, Mn^{2+}. The changes of the propagation vector from $\boldsymbol{k} = (1/2, 0, 1/2)$ in Sr_2MnMoO_6 and Sr_2MnWO_6 to $\boldsymbol{k} = (0, 1/2, 1/2)$ in Ca_2MnWO_6 are correlated with the changes observed in the unit-cell $\boldsymbol{a}$- and $\boldsymbol{b}$-parameters. A single-crystal neutron diffraction experiment seems to be necessary to remove the ambiguity in the magnetic structure determination.

Acknowledgments

We are grateful for the financial support of CICyT to the project MAT2001-0539, and we also to ILL for making all the facilities available.

Appendix

The possible magnetic structures compatible with the symmetry of the $P2_1/n$ space group have been determined by following the representation analysis technique described by Bertaut [21]. A small group $G_{\boldsymbol{k}}$ is constructed with those symmetry elements of $P2_1/n$ that leave the propagation vector $\boldsymbol{k}$ invariant. For Sr_2MnMoO_6 and Sr_2MnWO_6 the propagation vector is $\boldsymbol{k} = (1/2, 0, 1/2)$ and for Ca_2MnWO_6 it is $\boldsymbol{k} = (0, 1/2, 1/2)$. In both cases the small group coincides with the space group, $P2_1/n$. According to Kovalev [22], the irreducible representations of $G_{\boldsymbol{k}}$ for $\boldsymbol{k} = (1/2, 0, 1/2)$ and $(0, 1/2, 1/2)$ are those given in tables A.1 and A.2, respectively. A representation, Γ, is then constructed with the Fourier components, $\boldsymbol{m}^k$, corresponding to the Mn atoms of the 2d site. The Mn atoms are denoted as (1) $(1/2, 0, 0)$ and (2) $(0, 1/2, 1/2)$. This Γ representation is decomposed in terms of the irreducible representations of $G_{\boldsymbol{k}}$, and the corresponding basis vectors are determined by the projection operator method. The basis vectors for Sr_2MnMoO_6 and Sr_2MnWO_6 are shown in table A.1 and those of Ca_2MnWO_6 are shown in table A.2.

In these double-perovskite compounds, with a small distortion from the ideal cubic perovskite, it is worth determining the basis vectors that belong to the same multiplet of

Table A.2. Irreducible representations of the space group $P2_1/n$ for $\boldsymbol{k} = (0, 1/2, 1/2)$. The symmetry elements are written according to Kovalev's notation $\boldsymbol{\tau} = (1/2, 1/2, 1/2)$.

					Basis vectors	
	h_1	$h_{23}/(\boldsymbol{\tau})$	h_{25}	$h_{27}/(\boldsymbol{\tau})$	Mn1	Mn2
Γ^1	1	1	−1	−1	—	—
Γ^2	1	1	1	1	[1, 1, 1]	$[\bar{1}, 1, \bar{1}]$
Γ^3	1	−1	−1	1	—	—
Γ^4	1	−1	1	−1	[1, 1, 1]	$[1, \bar{1}, 1]$

the isotropic exchange Hamiltonian and, therefore, correspond to the same exchange energy. Therefore, the representation Γ must be considered as the direct product of the axial vector representation Γ^{axial} and the permutation representation Γ^{perm}. This means that

$$\Gamma = \Gamma^{perm} \times \Gamma^{axial}.$$

The representation Γ^{perm} can be decomposed in terms of the irreducible representations of $G_{\boldsymbol{k}}$ and Γ^{axial} can be decomposed in terms of the irreducible representations of the point group $g_{\boldsymbol{k}}$. This point group is formed by the same symmetry elements $(h/\boldsymbol{\tau})$ of $G_{\boldsymbol{k}}$, but excluding the translations $\boldsymbol{\tau}$. The characters of the irreducible representations Γ^i of $G_{\boldsymbol{k}}$ are related to those of $g_{\boldsymbol{k}}$, γ^i, by the expression

$$\Gamma^i(h/\boldsymbol{\tau}) = \exp(-\mathrm{i}\boldsymbol{k}\cdot\boldsymbol{\tau})\gamma^i(h).$$

For $\boldsymbol{k} = (1/2, 0, 1/2)$ the decompositions are

$$\Gamma^{perm} = \Gamma^2 + \Gamma^4 \qquad \text{and} \qquad \Gamma^{axial} = \gamma^1 + 2\gamma^3.$$

Each irreducible representation of Γ^{perm} generates a multiplet of the isotropic exchange Hamiltonian. So in this case there will be two multiplets

$$\Gamma^2 x(\gamma^1 + 2\gamma^3) = \Gamma^2 + 2\Gamma^4 \qquad \text{and} \qquad \Gamma^4 x(\gamma^1 + 2\gamma^3) = 2\Gamma^2 + \Gamma^4.$$

By taking into consideration the basis vectors given in table A.1, the basis vectors of the first multiplet $\Gamma^2 + 2\Gamma^4$ are

$$V_x^4 = m_{1x} - m_{2x}, \qquad V_y^2 = m_{1y} - m_{2y}, \qquad V_z^4 = m_{1z} - m_{2z}.$$

and those of $2\Gamma^2 + \Gamma^4$ are

$$V_x^2 = m_{1x} + m_{2x}, \qquad V_y^4 = m_{1y} + m_{2y}, \qquad V_z^2 = m_{1z} + m_{2z}.$$

For $\boldsymbol{k} = (0, 1/2, 1/2)$ the decomposition is

$$\Gamma^{perm} = \Gamma^2 + \Gamma^4 \qquad \text{and} \qquad \Gamma^{axial} = 2\gamma^2 + \gamma^4$$

and the multiplets of the isotropic exchange Hamiltonian are

$$\Gamma^2 x(2\gamma^2 + \gamma^4) = \Gamma^2 + 2\Gamma^4 \qquad \text{and} \qquad \Gamma^4 x(2\gamma^2 + \gamma^4) = 2\Gamma^2 + \Gamma^4.$$

According to table A.2, the basis vectors corresponding to the multiplet $\Gamma^2 + 2\Gamma^4$ are

$$V_x^4 = m_{1x} + m_{2x}, \qquad V_y^2 = m_{1y} + m_{2y}, \qquad V_z^4 = m_{1z} + m_{2z}$$

and for $2\Gamma^2 + \Gamma^4$ they are

$$V_x^2 = m_{1x} - m_{2x}, \qquad V_y^4 = m_{1y} - m_{2y}, \qquad V_z^2 = m_{1z} - m_{2z}.$$

If the anisotropic terms of the exchange Hamiltonian are negligible in comparison with the isotropic terms, it is possible to mix basis vectors belonging to different irreducible representations [23], but the basis vectors must belong to the same multiplet of the isotropic exchange Hamiltonian. One of the multiplets leads to a ferromagnetic coupling of the magnetic moments, $\boldsymbol{m}_1 = \boldsymbol{m}_2$ and the other to an antiferromagnetic one, $\boldsymbol{m}_1 = -\boldsymbol{m}_2$; in both cases a collinear magnetic structure is defined.

References

[1] Kusters R M, Singleton J, Keen D A, McGreevy R and Hayes W 1989 *Physica* B **155** 362
[2] Von Helmolt R, Wecker J, Holzapfel B, Schultz L and Samwer K 1993 *Phys. Rev. Lett.* **71** 2331
[3] Kobayashi K-I, Kimura T, Sawada H, Terakura K and Tokura Y 1988 *Nature* **395** 677
[4] Kobayashi K-I, Kimura T, Tomioka Y, Sawada H, Terakura K and Tokura Y 1999 *Phys. Rev.* B **59** 11 159
[5] García-Landa B, Ritter C, Ibarra M R, Blasco J, Algarabel P A, Mahendiran R and García J 1999 *Solid State Commun.* **110** 435
[6] Sarma D D, Sampathkumaran E V, Ray S, Nagarajan R, Majumdar S, Kumar A, Malini G and Guru Row T N 2000 *Solid State Commun.* **114** 465
[7] Gopalakrishnan J, Chattopadhyay A, Ogale S B, Venkatesan T, Greene R L, Millis A J, Ramesha K, Hannoyer B and Marest G 2000 *Phys. Rev.* B **62** 9538
[8] Niebieskikwiat D, Sánchez R D, Caneiro A, Morales L, Vasquez-Mansilla M, Rivadulla F and Hueso L E 2000 *Phys. Rev.* B **62** 3340
[9] Huang H Y, Cheong S W, Ong N P and Batlogg B 1996 *Phys. Rev. Lett.* **77** 2041
[10] Anderson M T, Greenwood K B, Taylor G A and Poeppelmeier K R 1993 *Prog. Solid State Chem.* **22** 197
[11] Patterson F K, Moeller C W and Ward R 1963 *Inorg. Chem.* **2** 196
[12] Galasso F, Douglas F and Kasper R J 1966 *Chem. Phys.* **44** 1672
[13] Chmaissen O, Kruk R, Dabrowski B, Brown D E, Xiong X, Kolesnik S, Jorgensen J D and Kimball C W 2000 *Phys. Rev.* B **62** 14 197
[14] Alonso J A, Casais M T, Martínez-Lope M J, Martínez J L, Velasco P, Muñoz A and Fernández-Díaz M T 2000 *Chem. Mater.* **12** 161
[15] Brixner L H 1960 *J. Phys. Chem.* **64** 165
[16] Itoh M, Ohta I and Inaguma Y 1996 *Mater. Sci. Eng.* B **41** 55
[17] Blasse G 1965 *Philips Res. Rep.* **20** 327
[18] Azad A K, Ivanov S A, Eriksson S-G, Rundlöf H, Eriksen J, Mathieu R and Svedlindh P 2001 *J. Magn. Magn. Mater.* **237** 124–34
[19] Azad A K, Ivanov S A, Eriksson S-G, Eriksen J, Rundlöf H, Mathieu R and Svedlindh P 2001 *Mater. Res. Bull.* **36** 2485
[20] Rodríguez-Carvajal J 1993 *Physica* B **192** 55
[21] Bertaut E F 1963 *Magnetism* vol 3, ed G T Rado and H Suhl (New York: Academic) ch 4
[22] Kovalev O K 1993 *Representation of the Crystallographic Space Groups* 2nd edn, ed H T Stokes and D M Hatch (London: Gordon and Breach)
[23] Izyumov Yu A, Naish E V and Ozerov R P 1991 *Neutron Diffraction of Magnetic Materials* (New York: Plenum)